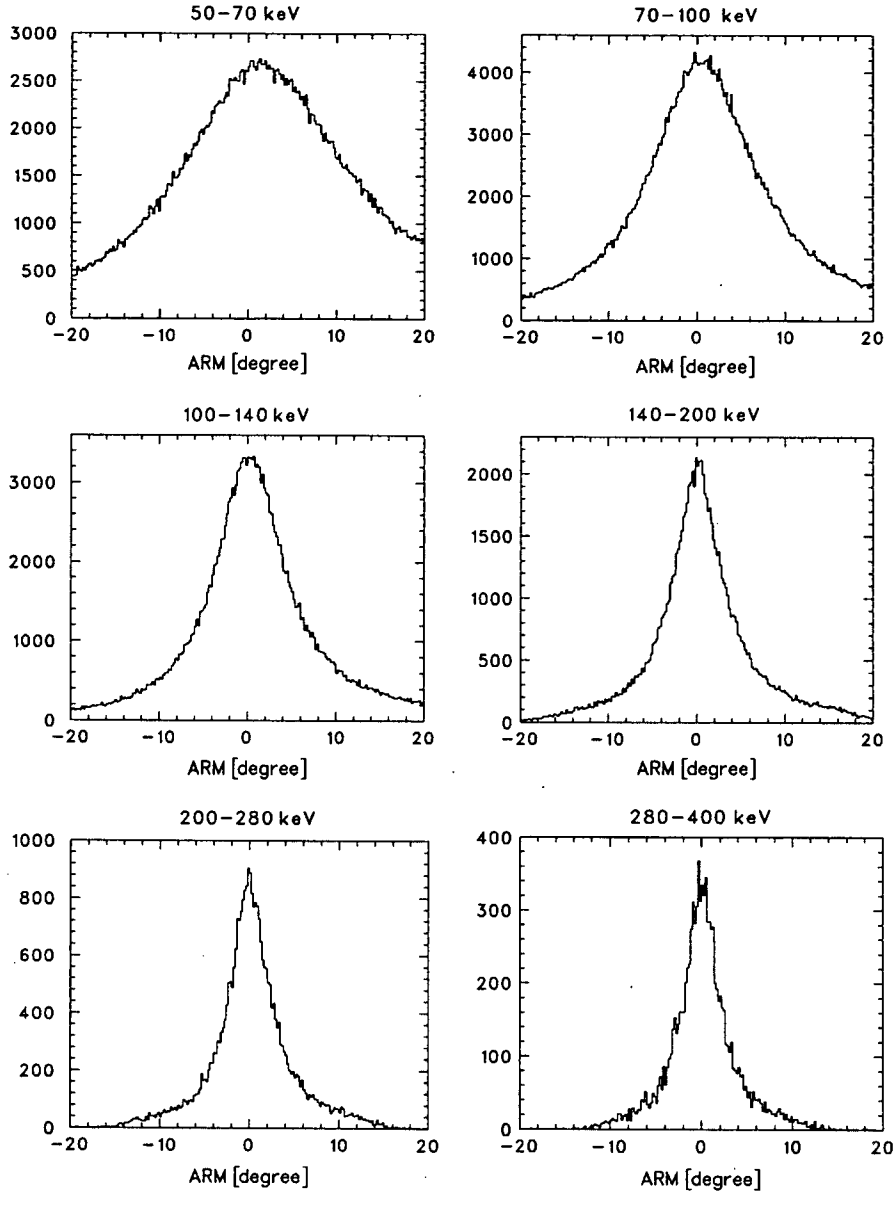

Fig. 9. Distribution of the ARM ($\Delta\theta = \theta_{energy} - \theta_{geom}$), in the six energy bands.

"DSSD–CdTe Bottom" and the "DSSD–CdTe Side" events. As noted later in this section, the CdTe scattered events significantly deteriorate the angular resolution due to its large Doppler broadening.

The FWHM of the ARM distribution is one indicator of the angular resolution. The thick solid line in Fig. 10 shows the FWHM of the ARM distribution, $\Delta\theta_{total}$, as a function of the incident energy. As the energy increases, the angular resolution becomes better. It amounts to 9° at 120 keV, and 4.4° at 330 keV.

The distribution of the ARM originates from three main components: the position resolution, the energy resolution, and the Doppler broadening. Using the case of the energy band from 140 to 200 keV, we present every contribution separately by calculating the ARMs including each effect in Fig. 11. The distributions of scatter caused by the position resolution ($\Delta\theta_{pos}$) and that by the energy resolution ($\Delta\theta_{ene}$) are Gaussian-like. In contrast, that of the Doppler broadening effect ($\Delta\theta_{DB}$) has a narrow peak with broad non-Gaussian wings. Because the effect of these wings is significant when the three components are convoluted, the FWHM of the $\Delta\theta_{DB}$ distribution underestimates the contribution of the Doppler broadening effect. In order to avoid this problem, we redefined the contribution from the Doppler broadening effect as

$$\Delta\theta_{DB} = \sqrt{(\Delta\theta_{total})^2 - (\Delta\theta_{pos})^2 - (\Delta\theta_{ene})^2}. \quad (3)$$

Please note that the redefined $\Delta\theta_{DB}$ is not independent of the position and energy resolutions of the detectors.

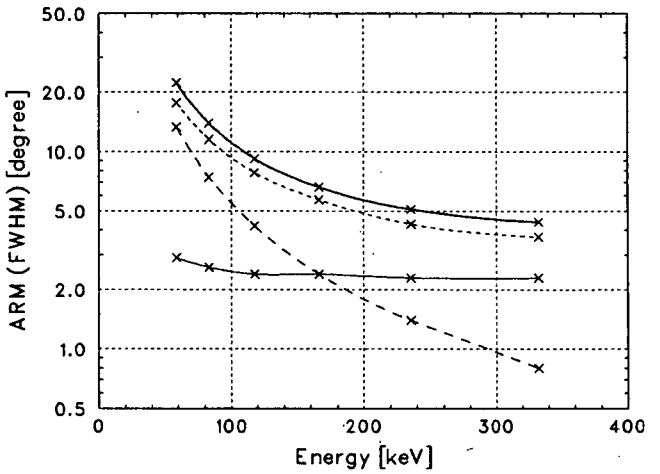

Fig. 10. FWHM of the ARM ($\Delta\theta_{tot}$: thick solid line) as a function of the incident photon energy. Contributions by the energy resolution ($\Delta\theta_{ene}$: dashed), by the position resolution ($\Delta\theta_{pos}$: thin solid line), and by the Doppler broadening effect ($\Delta\theta_{DB}$: dotted line) are also presented. See text for detail.

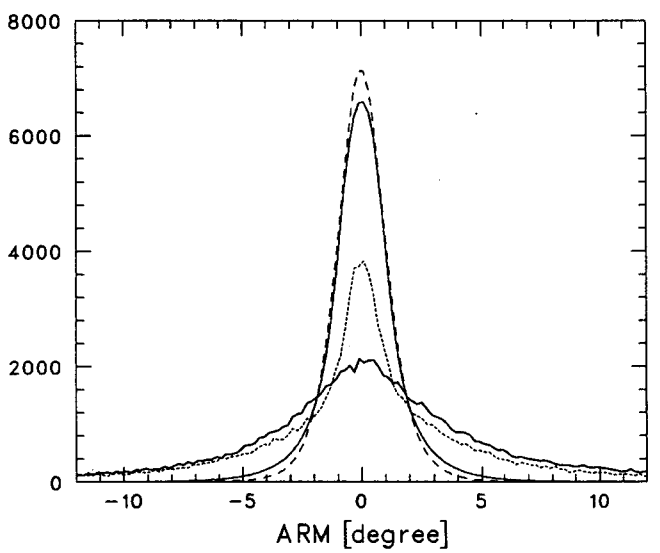

Fig. 11. The ARM distribution profile in the energy band from 140 to 200 keV (thick solid line). Contributions by the energy resolution ($\Delta\theta_{ene}$: dashed line), by the position resolution ($\Delta\theta_{pos}$: thin solid line), and by the Doppler broadening effect ($\Delta\theta_{DB}$: dotted line) are also presented.

The three components thus defined as a function of the incident energy are superposed in Fig. 10. The contribution from the Doppler broadening is a major component in all energy bands. Below 100 keV, the energy resolution limits the angular resolution. In the energy range higher than 200 keV, the angular resolution is limited mainly by the position resolution of the detector. If we are able to prepare CdTe pixel detectors with the finer pixel pitch of 400 μm, the same as that of the DSSDs, the FWHM of the ARM distribution is greatly improved from 4.4° to 2.6° at 330 keV. Note that this significant improvement is achieved

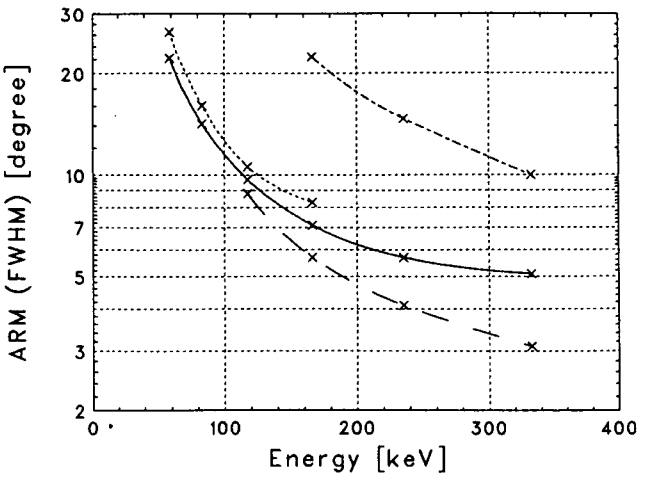

Fig. 12. The ARM of various hit positions: "DSSD–DSSD" events (dotted), "DSSD–CdTe Bottom" events (dashed), "DSSD–CdTe Side" events (solid), and "CdTe Bottom–CdTe Bottom" events (dotdash) are presented.

because the position resolution becomes smaller than the core of the Doppler broadening.

Fig. 12 shows the angular resolution for the various event types classified by hit positions (described in Section 4). We find that "DSSD–CdTe Bottom" events give the best angular resolution. At 330 keV, FWHM of the ARM with these events is 3.1°. In contrast, since the Doppler broadening of CdTe is large, CdTe detectors are not suitable as scatterers for high angular resolution Compton cameras. For example, the ARM of "CdTe Bottom–CdTe Bottom" events is significantly worse when compared to the DSSD-scattered events.

6. Conclusion

We carried out Monte Carlo simulations to evaluate the performances of the proposed narrow-FOV Si/CdTe Compton telescope, the SGD, for the NeXT mission. The detection efficiency in the Compton mode at ~100 keV is more than 10%. It is shown that the CdTe Side detectors play an important role in achieving better detection efficiency at ~100 keV. A few degrees of the angular resolution is obtained due to the small Doppler broadening effect of Si, combined with the high energy and position resolution of both the DSSDs and CdTe pixel detectors. At 330 keV, FWHM of ARM is 4.4 keV and it is improved to 3.1° if "DSSD–CdTe Bottom" events are selected. This result is the same level of the proposed Advanced Compton Telescope, which has an angular resolution of 3.3° at ~300 keV [22]. Since our detector is optimized for a lower energy band compared with other Compton telescopes, Compton reconstruction works with the Si/CdTe Compton telescope at lower energy such as ~80 keV. For example, an angular resolution of 9° is obtained for gamma-rays with an energy of 120 keV, which is very low for a Compton

telescope. For the next step, studies of activation backgrounds caused by cosmic rays in orbit and the evaluation of the capability to reject such backgrounds is indispensable to determine detailed parameters of the detector. A Geant4 based Monte Carlo program with a capability to handle activation in the material is now being set up.

References

[1] V. Schönfelder, et al., ApJ Suppl. 86 (1993) 657.
[2] V. Schönfelder, et al., Astron. Astrophys. Suppl. 120 (1996) 13.
[3] V. Schönfelder, et al., Astron. Astrophys. Suppl. 143 (2000) 145.
[4] V. Schönfelder, New Astron. Rev. 48 (2004) 193.
[5] T. Kamae, R. Enomoto, N. Harada, Nucl. Instr. and Meth. A 260 (1987) 254.
[6] Y.F. Du, Z. He, G.F. Knoll, D.K. Wehe, W. Li, Nucl. Instr. and Meth. A 457 (2001) 203.
[7] J.D. Kurfess, W.N. Johnson, R.A. Kroeger, B.F. Phlips, E.A. Wulf, Nucl. Instr. and Meth. A 505 (2003) 256.
[8] T.J. O'Neill, D. Bhattacharya, M. Polsen, A.D. Zych, J. Samimi, A. Akyuz, IEEE Trans. Nucl. Sci. NS-50 (2003) 251.
[9] T. Takahashi, K. Nakazawa, T. Kamae, H. Tajima, Y. Fukazawa, M. Nomachi, M. Kokubun, Proc. SPIE 4851 (2003) 1228.
[10] G. Kanbach, et al., New Astron. Rev. 48 (2004) 275.
[11] T. Tanaka, et al., Proc. SPIE 5501 (2004) 229.
[12] S. Watanabe, et al., IEEE Trans. Nucl. Sci. NS-52 (2005) 2045.
[13] T. Tanaka, et al., Nucl. Instr. and Meth. A 568 (2006) 375.
[14] T. Takahashi, K. Mitsuda, H. Kunieda, Proc. SPIE 6266 (2006) 62660D.
[15] H. Tajima, et al., IEEE Trans. Nucl. Sci. NS-52 (2005) 2749.
[16] T. Takahashi, et al., Proc. SPIE 5488 (2004) 549.
[17] S. Takeda, et al., Nucl. Instr. and Meth. A (2007).
[18] Geant4, (http://geant4.web.cern.ch/geant4/).
[19] G4LECS, (http://public.lanl.gov/mkippen/actsim/g4lecs/).
[20] R.M. Kippen, New Astron. Rev. 48 (2004) 221.
[21] A. Zoglauer, G. Kanbach, Proc. SPIE 4851 (2003) 1302.
[22] S.E. Boggs, et al., The Advanced Compton Telescope Mission, astro-ph/0608532, (2006).

Japanese Journal of Applied Physics
Vol. 46, No. 9A, 2007, pp. 6043–6045

New CdTe Pixel Gamma-Ray Detector with Pixelated Al Schottky Anodes

Shin WATANABE[1,2*], Shin-nosuke ISHIKAWA[1,2], Shin'ichiro TAKEDA[1,2], Hirokazu ODAKA[1,2], Takaaki TANAKA[3], Tadayuki TAKAHASHI[1,2], Kazuhiro NAKAZAWA[2], Masaaki YAMAZATO[4], Akira HIGA[4], and Sakari KANEKU[5]

[1]*Institute of Space and Astronautical Science, Japan Aerospace Exploration Agency, 3-1-1 Yoshinodai, Sagamihara, Kanagawa 229-8510, Japan*
[2]*Department of Physics, The University of Tokyo, Bunkyo, Tokyo 113-0033, Japan*
[3]*Stanford Linear Accelerator Center, Menlo Park, CA 94025, U.S.A.*
[4]*Faculty of Engineering, University of the Ryukyus, 1 Senbaru, Nishihara, Okinawa 930-0213, Japan*
[5]*ACRORAD Co., Ltd., Uruma, Okinawa 904-2234, Japan*

(Received May 9, 2007; accepted May 25, 2007; published online September 7, 2007)

We developed a new Al Schottky CdTe pixel detector and measured its spectral performance. It has pixelated anodes made of aluminum and a common cathode made of platinum. Because of the low leakage current and the high bias voltage owing to the Schottky diode characteristic and the anode pixel configuration, a good spectral performance including a high energy resolution was achieved. When the pixel detector with a thickness of 0.75 mm was subjected to a bias voltage of 400 V and was operated at −20 °C, the full-width-half-maximum (FWHM) energy resolution of 1.1 and 1.8 keV at 59.5 and 122 keV, respectively, were successfully obtained. The spectral performance obtained with the Al Schottky CdTe pixel detector exceeded that obtained with the conventional In Schottky CdTe pixel detector, which has an In common anode and Pt pixelated cathodes, under the same operating conditions. [DOI: 10.1143/JJAP.46.6043]

KEYWORDS: gamma-ray detector, cadmium telluride (CdTe), pixel detector

1. Introduction

Hard X-ray and gamma-ray imaging spectrometers with good spatial and energy resolutions are desired for medical, industrial and astrophysical applications. Cadmium telluride (CdTe) and cadmium zinc telluride (CZT) are very promising materials as hard X-ray and gamma-ray imaging spectrometers, because they have a high detection efficiency comparable to that of NaI scintilators and have a good energy resolution comparable to that of Ge detectors. Although a weak point of CdTe and CZT was the degradation of energy resolution and peak detection efficiency owing to poor charge transport properties of their materials, several techniques have been developed to maintain good spectral performance.[1,2)]

In recent years, we have successfully overcome the poor charge transport properties by adopting a thin CdTe diode device. The basic idea of using a CdTe diode is to utilize indium (In) as the anode electrode on a p-type CdTe wafer and platinum (Pt) as the cathode.[1,3,4)] A high Schottky barrier formed on the In/p-CdTe interface leads us to the use of the detector as a diode. Using this type of detector with a thickness of 0.5 mm at an applied bias voltage as high as 1 kV, we have obtained high energy resolutions: 830 eV (full-width-half-maximum: FWHM) at 59.5 keV and 2.1 keV (FWHM) at 662 keV.[1,4)]

On the basis of the In Schottky diode device, we have developed CdTe diode pixel detectors, utilizing In as the common anode and Pt as the pixelated cathode (In/CdTe/Pt-pixel).[4–6)] Because of their Schottky diode characteristic, low leakage current and good energy resolution have been achieved from the In/CdTe/Pt-pixel configuration. Ideally, electrons, which have a larger mobility and a longer lifetime than holes in CdTe, have to be collected for high energy resolution, therefore, the anode side should be pixelated. However, with the current electrode technology, it is difficult to divide an In electrode into pixels.

Recently, as an electrode material, aluminum (Al) has been found to be a good alternative to In.[7,8)] In addition to low leakage current and high energy resolution comparable to those of In/CdTe/Pt detectors, Al/CdTe/Pt detectors have an advantage that an Al anode can be divided into pixels. Therefore, it is possible to fabricate electron-collecting-type diode pixel detectors, utilizing Al as pixelated anodes and Pt as the common cathode (Al-pixel/CdTe/Pt).

We have constructed the first Al-pixel/CdTe/Pt detector using the same components as those used in our recent In/CdTe/Pt-pixel detectors. In this paper, we report the achieved performance of the Al-pixel/CdTe/Pt detector. A comparison between the Al-pixel/CdTe/Pt and In/CdTe/Pt-pixel detectors is also described.

2. Setup of the Al Schottky CdTe Pixel Detector

Figure 1 shows a picture of the Al-pixel/CdTe/Pt detector together with the In/CdTe/Pt-pixel detector. The CdTe device has a size of $13.35 \times 13.35\,mm^2$ and a thickness of 0.75 mm. The CdTe crystal is manufactured

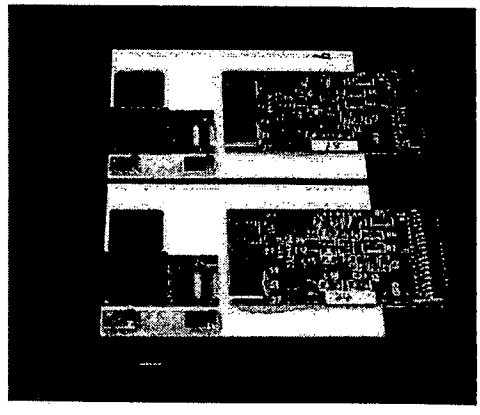

Fig. 1. Picture of the CdTe pixel detectors. The bottom shows the Al-pixel/CdTe/Pt detector and the top shows the In/CdTe/Pt-pixel detector.

*E-mail address: watanabe@astro.isas.jaxa.jp

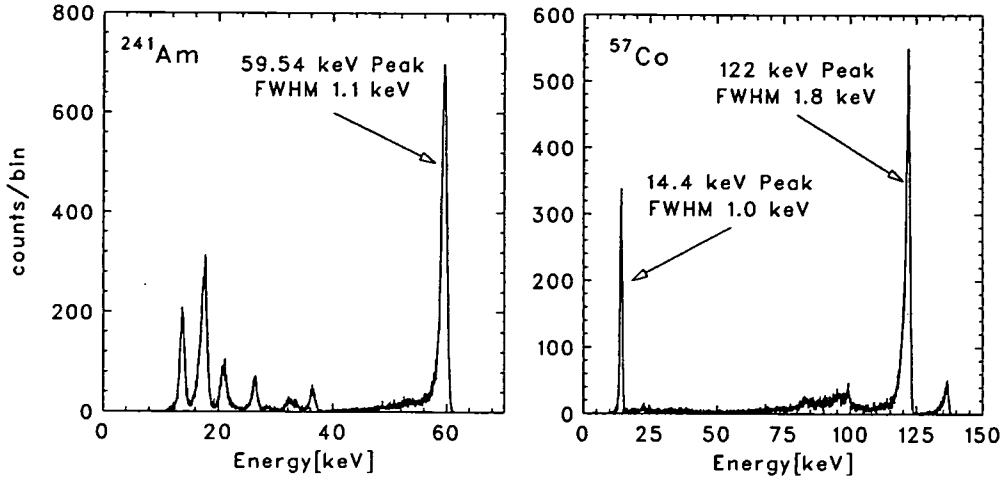

Fig. 2. ^{241}Am and ^{57}Co spectra obtained with one pixel of the Al/CdTe/Pt-pixel detector. The operating temperature was −20 °C, and, the applied bias voltage was −400 V for the Pt common electrode. The achieved FWHM energy resolutions were 1.0, 1.1, and 1.8 keV at 14.4, 59.5, and 122 keV, respectively.

by ACRORAD in Japan using the traveling heater method (THM). The Pt side is used as the common electrode and the Al side is divided into 8 × 8 = 64 pixels. The pixel size is 1.35 × 1.35 mm^2, and the gap between the pixel electrode is 50 μm. Around the pixels, a guard ring electrode with a width of 1 mm is attached. Additionally, a thin layer of gold is evaporated on the Al pixel side to ensure a good bump bonding connectivity.

The procedure for the component mounting is the same as that for In/CdTe/Pt-pixel detectors.[6] ASIC for both pixel detectors readout is VA64TA, which was developed by this research team in conjunction with IDEAS and SLAC.[9]

3. Spectral Performance of the Al Schottky CdTe Pixel Detector

In order to evaluate the spectral performance of the Al-pixel/CdTe/Pt detector, we operated the detector in a thermostatic chamber at −20 °C. The applied bias voltage was −400 V for the Pt common cathode. Spectroscopy measurements were performed using gamma-rays from ^{241}Am and ^{57}Co sources.

The spectra obtained from one of the pixels with the best performance are shown in Fig. 2. High energy resolutions were obtained: 1.0 keV (FWHM) at 14.4 keV, 1.1 keV (FWHM) at 59.5 keV, and 1.8 keV (FWHM) at 122 keV. Figure 3 shows the distribution of energy resolution from all 64 pixels. The FWHM spread is within about 10% for almost all pixels. The energy resolutions in the summed spectrum of all 64 pixels were 1.3 keV (FWHM) and 2.0 keV (FWHM) at 59.5 keV and 122 keV, respectively. Additionally, it was found that the long-term stability in the spectrum is sufficient for practical use under our operating conditions. Any significant deteriorations in energy resolution and detection efficiency have not been observed for at least one hour after applying bias voltage.

4. Comparison between the Two Types of CdTe Diode Pixel Detectors

In order to study the effect of the spectral response on the difference in electrode configuration between the Al-pixel/CdTe/Pt and In/CdTe/Pt-pixel detectors, both types of

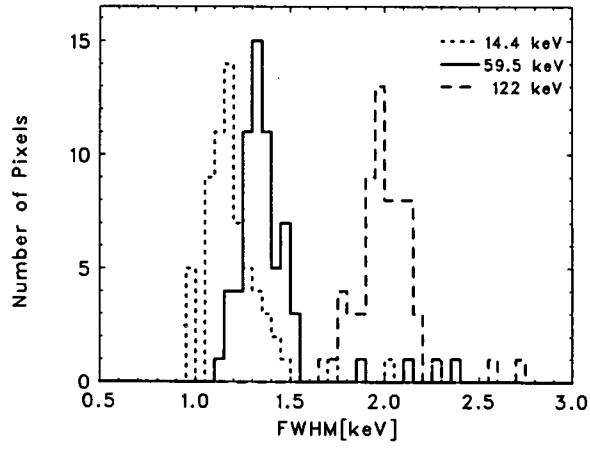

Fig. 3. Distribution of energy resolution from all 64 pixels of the Al-pixel/CdTe/Pt detector.

CdTe device with the same dimension (13.35 × 13.35 × 0.75 mm^3) were prepared (Fig. 1). The detectors were operated at −20 °C. We examined the changes of the spectral shape in the 122 keV peak from a ^{57}Co source at various bias voltages.

Figure 4 shows the peak shapes for 122 keV gamma-ray photons obtained using the two types of pixel detector. The sums of the spectra from all pixels are shown. The applied bias voltages are from −100 to −400 V for the Al-pixel/CdTe/Pt detector, and from 100 to 1000 V for the In/CdTe/Pt-pixel detector. The energy scales of the two detector are calibrated on the basis of the spectra of −400 and 1000 V bias, respectively.

In order to quantify the peak heights and the lower tail amounts, the ratios of 120–124 keV count rate to 110–124 keV count rate are plotted as a function of applied bias voltage in Fig. 5. The filled circles and the open circles show the data of Al-pixel/CdTe/Pt and In/CdTe/Pt-pixel detectors, respectively. A higher ratio means a sharper peak and a smaller tail.

Compared with the case of using the In/CdTe/Pt-pixel detector, a small tail and a high peak can be obtained with

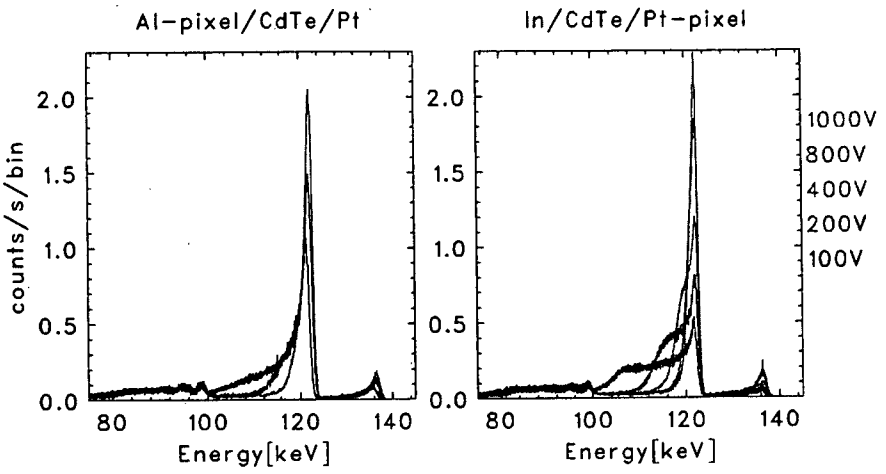

Fig. 4. Spectral changes of the 122 keV peak that are caused by the bias voltage. Left: Spectra obtained with the Al-pixel/CdTe/Pt detector. Bias voltages of −100, −200, and −400 V were applied to the Pt common cathode. Right: Spectra obtained with the In/CdTe/Pt-pixel detector. Bias voltages of 100, 200, 400, 800, and 1000 V were applied to the In common anode. Both detectors were operated at −20 °C. The thickness of the detectors was 0.75 mm. The spectra from all pixels were summed. The energy scales of Al-pixel/CdTe/Pt and In/CdTe/Pt-pixel were calibrated on the basis of the spectra of −400 and 1000 V bias, respectively.

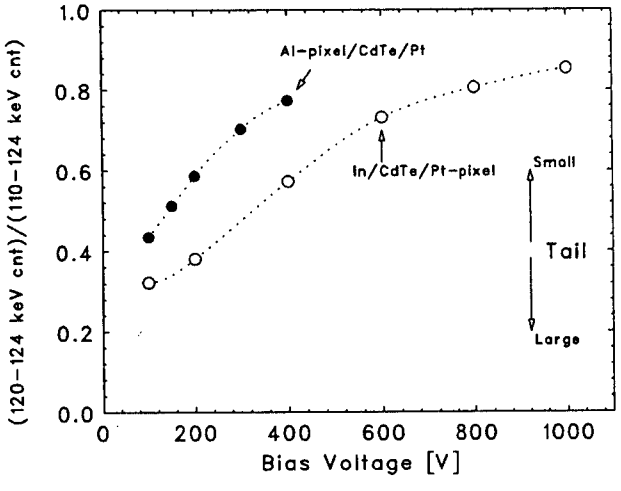

Fig. 5. Characteristics of 122 keV peak shapes. The ratios of 120–124 keV count rate to 110–124 keV count rate are plotted as a function of bias voltage. Filled circles show the data obtained using the Al-pixel/CdTe/Pt detector, and open circles show the data obtained using the In/CdTe/Pt-pixel detector.

the Al-pixel/CdTe/Pt detector under the same bias voltage condition. The peak obtained with the Al-pixel/CdTe/Pt detector under the bias voltage of −400 V is almost equivalent to the peak obtained with the In/CdTe/Pt-pixel detector under the bias voltage of 800 V. The spectral difference should be caused by the $\mu\tau$ product difference between electrons and holes in the CdTe crystal (μ, mobility; τ, lifetime). In the THM CdTe crystals manufactured by ACRORAD, the $\mu\tau$ product of electrons is 10–30 times larger than that of holes.[10] In the case of using the Al-pixel/CdTe/Pt detector, because electrons incoming to the pixel electrodes produce a large part of the signal, there is an advantage in spectral performance. On the other hand, in the case of using the In/CdTe/Pt-pixel detector, small $\mu\tau$ holes should be moved to the cathode pixels. Therefore, a higher bias voltage was required for obtaining a good spectral performance.

5. Conclusions

We have constructed a new type of CdTe pixel diode detector with a Pt common cathode and Al pixelated anodes. The construction procedure was the same as that for our conventional CdTe pixel diode detector with an In common anode and Pt pixelated cathodes. When we applied a bias voltage of 400 V to a 0.75-mm-thick detector and operated at −20 °C, the pixel detector worked successfully and a good energy resolution was achieved. The obtained energy resolutions of one pixel were 1.1 keV (FWHM) at 59.5 keV and 1.8 keV (FWHM) at 122 keV under these conditions. Additionally, we compared the spectral performance between the Al-pixel/CdTe/Pt and In/CdTe/Pt-pixel detectors. It was found that a better energy resolution can be obtained with the Al-pixel/CdTe/Pt detector than with the In/CdTe/Pt-pixel detector under the same bias voltage condition.

1) T. Takahashi and S. Watanabe: IEEE Trans. Nucl. Sci. **48** (2001) 950.
2) O. Limousin: Nucl. Instrum. Methods Phys. Res., Sect. A **504** (2003) 24.
3) T. Takahashi, B. Paul, K. Hirose, C. Matsumoto, R. Ohno, T. Ozaki, K. Mori, and Y. Tomita: Nucl. Instrum. Methods Phys. Res., Sect. A **436** (1999) 111.
4) T. Takahashi, S. Watanabe, G. Sato, Y. Okada, S. Kubo, Y. Kuroda, M. Onishi, and R. Ohno: IEEE Trans. Nucl. Sci. **48** (2001) 287.
5) T. Mitani, T. Tanaka, K. Nakazawa, T. Takahashi, T. Takashima, H. Tajima, H. Nakamura, M. Nomachi, T. Nakamoto, and Y. Fukazawa: IEEE Trans. Nucl. Sci. **51** (2004) 2432.
6) S. Watanabe, S. Takeda, S. Ishikawa, H. Odaka, M. Ushio, T. Tanaka, K. Nakazawa, T. Takahashi, H. Tajima, Y. Fukazawa, Y. Kuroda, and M. Onishi: to be published in Nucl. Instrum. Methods Phys. Res., Sect. A.
7) H. Toyama, A. Nishihira, M. Yamazato, A. Higa, T. Maehama, R. Ohno, and M. Toguchi: Jpn. J. Appl. Phys. **43** (2004) 6371.
8) H. Toyama, M. Yamazato, A. Higa, T. Maehama, R. Ohno, and M. Toguchi: Jpn. J. Appl. Phys. **44** (2005) 6742.
9) T. Tanaka, S. Watanabe, S. Takeda, K. Oonuki, T. Mitani, K. Nakazawa, T. Takashima, T. Takahashi, H. Tajima, N. Sawamoto, Y. Fukazawa, and M. Nomachi: Nucl. Instrum. Methods Phys. Res., Sect. A **568** (2006) 375.
10) G. Sato, T. Takahashi, M. Sugiho, M. Kouda, T. Mitani, K. Nakazawa, Y. Okada, and S. Watanabe: IEEE Trans. Nucl. Sci. **49** (2002) 1258.

Journal of Nuclear and Radiochemical Sciences, Vol. 8, No. 2, pp. 55-58, 2007

Development of Gas-jet Transport System Coupled to the RIKEN Gas-filled Recoil Ion Separator GARIS for Superheavy Element Chemistry

H. Haba,*[,a] D. Kaji,[a] H. Kikunaga,[a] T. Akiyama,[a,b] N. Sato,[a,c] K. Morimoto,[a] A. Yoneda,[a] K. Morita,[a] T. Takabe,[d] and A. Shinohara[d]

[a]*Nishina Center for Accelerator Based Science, RIKEN, Wako, Saitama 351-0198, Japan*
[b]*Department of Physics, Saitama University, Sakura, Saitama 338-8570, Japan*
[c]*Department of Physics, Tohoku University, Aoba, Sendai 980-8578, Japan*
[d]*Graduate School of Science, Osaka University, Toyonaka, Osaka 560-0043, Japan*

Received: January 27, 2007; In Final Form: April 3, 2007

A gas-jet transport system for the superheavy element chemistry was coupled to the gas-filled recoil ion separator GARIS at the RIKEN Linear Accelerator. The performance of the system was investigated using ^{206}Fr and ^{245}Fm produced in the ^{40}Ar-induced reactions on ^{169}Tm and ^{208}Pb targets, respectively. Alpha particles of ^{206}Fr and ^{245}Fm separated with GARIS and transported by the gas-jet were measured with a rotating wheel system for α spectrometry under low background condition. The high gas-jet efficiency of over 80% was found to be independent of the beam intensity up to 2 particle μA. These results suggest that the GARIS/gas-jet system is a promising tool for future superheavy element chemistry at RIKEN.

1. Introduction

The chemistry of the superheavy elements (SHEs) with atomic numbers $Z \geq 104$ has become one of the most exciting and challenging research subjects in nuclear and radiochemistry.[1,2] Experimental studies on chemical properties of SHEs have been performed for elements 104 to 108 and very recently element 112.[1,2] The production rates of the SHE nuclides, however, are extremely low, i.e., atoms per minute for elements 104 (Rf) and 105 (Db) down to atoms per hour or day for elements 106 (Sg) to 108 (Hs),[2] and their half-lives are less than ~1 min. This situation forces us to perform rapid and efficient on-line chemical experiments with "single atoms" using heavy-ion accelerators. The gas-jet transport technique has been commonly used to transfer SHE atoms from a target chamber to various chemistry apparatuses. Here, nuclear reaction products recoiling out of a target are stopped in the chamber filled with helium gas, and are often attached to aerosol particles such as potassium chloride (KCl) and carbon. The gas and activity-laden aerosol particles are swept out through a capillary to a distant site where chemistry apparatuses and detectors are equipped.

SHE atoms are produced among large amounts of background radioactivities which hinder the detection of decay signals of SHE nuclides. Recently available high-intensity beams of more than 1 particle μA (pμA) also give rise to a serious problem in that the plasma formed by the beam in the target chamber significantly reduces the gas-jet transport efficiency. To overcome these situations, it has been proposed that a recoil separator for nuclear physics research on SHEs should be coupled to the chemistry system with the aid of the gas-jet transport technique mentioned above.[1,3] With this method, background radioactivities originating from other reaction products are largely removed. The high and stable gas-jet efficiencies are obtained owing to the condition free from plasma. Furthermore, chemical reactions of various compounds can be studied by directly feeding complexing reagents into the gas-jet chamber without aerosol materials. The first experiment with the recoil transfer chamber (RTC) coupled to the Berkeley Gas-filled Separator (BGS) was very successful.[4,5] The isotope of ^{257}Rf physically separated from the large amount of β-decaying products was identified with a liquid scintillator after a liquid-liquid solvent extraction. Thereafter, the BGS/RTC system was used in the model experiments of Rf (References 6–8) and Hs (Reference 9). At Gesellschaft für Schwerionenforschung (GSI), the components of the former HElium Charge-exchange Kaleidoscope (HECK) separator are being used to set up a dedicated separator for the SHE chemistry.[3]

In the RIKEN Linear Accelerator (RILAC) facility, the gas-filled recoil ion separator GARIS has been used to search for the heaviest SHE nuclides.[10–13] The isotopes of ^{271}Ds, ^{272}Rg, and ^{277}112 found at GSI were confirmed with better statistics and with new spectroscopic information,[10–12] and a new isotope of element 113, ^{278}113, was successfully synthesized.[13] GARIS is expected to give us low background condition and high transport efficiencies for SHEs. In this work, we have installed a gas-jet transport system at the focal plane of GARIS to start the SHE chemistry in RIKEN. The performance of the system was appraised using ^{206}Fr and ^{245}Fm produced in the ^{169}Tm(^{40}Ar,3n)^{206}Fr and ^{208}Pb(^{40}Ar,3n)^{245}Fm reactions, respectively.

2. Experimental

A schematic of the experimental setup is shown in Figure 1. The ^{40}Ar^{9+} ion beam was extracted from RILAC. The metallic ^{169}Tm and ^{208}Pb targets of 120 and 420 μg cm^{-2} thicknesses, respectively, were prepared by vacuum evaporation on 30 μg cm^{-2} carbon backing foils. Sixteen targets were mounted on a rotating wheel of 30 cm in diameter. The wheel was rotated during the irradiation at 3000 rpm. The beam energies were 169.7 MeV for ^{169}Tm and 198.6 MeV for ^{208}Pb at the middle of the targets. At these incident energies, the cross section for the ^{169}Tm(^{40}Ar,xn)$^{209-x}$Fr reactions (x = 2 + 3) is 376 ± 7 μb,[14] while that for ^{208}Pb(^{40}Ar,3n)^{245}Fm is 15 ± 5 nb.[15] The beam intensity was monitored by measuring elastically scattered projectiles with a Si PIN photodiode (Hamamatsu S1223) mounted at 45° with respect to the beam axis. The typical beam intensity was 2 pμA. GARIS was filled with helium at a pressure of 88 Pa.

*Corresponding author. E-mail: haba@riken.jp. Fax: +81-48-461-5301.

Published on Web 10/19/2007

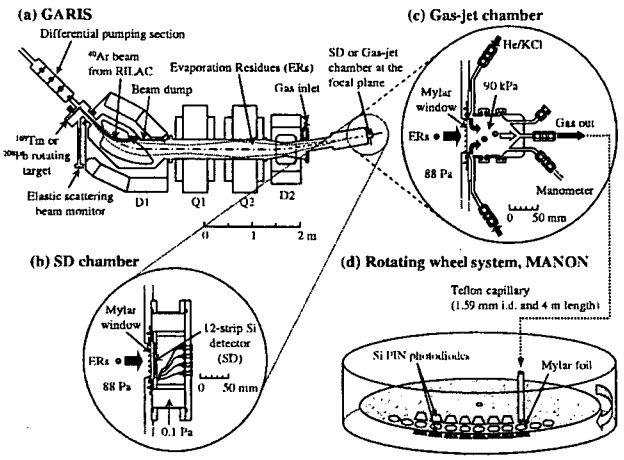

Figure 1. A schematic of the experimental setup: (a) RIKEN gas-filled recoil ion separator GARIS; (b) 12-strip Si detector (SD) chamber; (c) Gas-jet chamber coupled to GARIS; (d) Rotating wheel system MANON for α spectrometry.

The magnetic rigidities were set at 1.64 Tm for ^{206}Fr and at 2.01 Tm for ^{245}Fm. The other details of GARIS are given elsewhere.[11]

As shown in Figures 1(a) and 1(b), the evaporation residues of interest were separated in-flight from beam particles and transfer reaction products with GARIS, and were implanted into a 12-strip Si detector (SD) of 60 × 60 mm^2 (Hamamatsu 12CH PSD) through a Mylar window of 3.5 ± 0.1 μm thickness which was supported with a stainless-steel honeycomb grid with 92.5% transparency and of 60 mm diameter. Alpha-particle measurements of ^{206}Fr were conducted for 2600 s under the beam-on condition and for 300 s after a 30-s beam irradiation. In the ^{245}Fm experiment, the cycle of the beam-on (5 s) and beam-off (15 s) measurements was repeated 1265 times, because no α peak of ^{245}Fm was observed in the beam-on spectrum due to large amounts of background events. The α-particle energy resolution of SD was 50 keV FWHM. All events were registered in an event-by-event mode.

In the gas-jet transport experiments, ^{206}Fr and ^{245}Fm separated by GARIS were guided into the gas-jet chamber of 60 mm length as shown in Figure 1(c). The reaction products were stopped in the helium gas at 90 kPa, attached to KCl aerosol particles generated by sublimation of the KCl powder at 620 °C, and were continuously transported through a Teflon capillary (1.59 mm i.d., 4 m length) to the rotating wheel system MANON for α spectrometry (Figure 1(d)) which was the compact one of the Measurement system for the Alpha-particle and spontaneous fissioN events ON-line developed at Japan Atomic Energy Agency (JAEA).[16] The flow rate of the helium gas was 5 L min^{-1}. In the ^{206}Fr experiment, the temperature of the KCl aerosol generator was varied from 540 to 640 °C in steps of about 20 °C to optimize the gas-jet transport efficiency. In MANON, aerosol particles were deposited on Mylar foils of 0.68 μm thickness and 20 mm diameter placed at the periphery of a 40-position stainless steel wheel of 420 mm diameter. The wheel was stepped at 30-s and 2-s intervals for ^{206}Fr and ^{245}Fm, respectively, to position the foils between seven pairs of Si PIN photodiodes (Hamamatsu S3204-09). Each detector had an active area of 18 × 18 mm^2 and a 38% counting efficiency for α particles. The α-particle energy resolution was 60 keV FWHM for the detectors which look at the sample from the collection side (top detectors).

3. Results and Discussion

Figure 2(a) shows an α-particle spectrum measured in the ^{206}Fr experiment for 2600 s in the 6th strip (middle) of SD under the beam-on condition. Alpha peaks of ^{206}Fr ($T_{1/2}$ = 15.9 s, E_α = 6.790 MeV)[17] and ^{205}Fr (3.85 s, 6.915 MeV)[17] and of their daughter nuclides ^{202}At (182 s, 6.135 MeV; 184 s, 6.228 MeV)[17] and ^{201}At (89 s, 6.344 MeV)[17] were identified. The broad component above 7 MeV is associated with the implantation of evaporation residues (ERs) and target recoils (TRs). Figure 2(b) shows an α-particle spectrum measured in the 6th strip of SD for 300 s after the 30-s beam irradiation. The decay curve of the 6.790-MeV α peak of ^{206}Fr is shown in the inset of Figure 2(b). The half-life of ^{206}Fr was determined to be 15.3 ± 0.2 s, which is in agreement with the literature value of 15.9 ± 0.2 s (Reference 17) within 2σ. The contribution of the α particles of ^{207}Fr (14.8 s, 6.768 MeV)[17] produced in the ^{169}Tm(^{40}Ar,2n)^{207}Fr reaction to the 6.790-MeV peak of ^{206}Fr is found to be negligible from the absence of the 6.087-MeV peak of its daughter nuclide ^{203}At (7.4 min, 6.087 MeV)[17] in Figure 2(a). On the other hand, the α-particle spectrum measured in the first top detector of MANON for 30 s after the 30-s aerosol collection is compared in Figure 2(c). The α peak of ^{206}Fr is clearly seen in

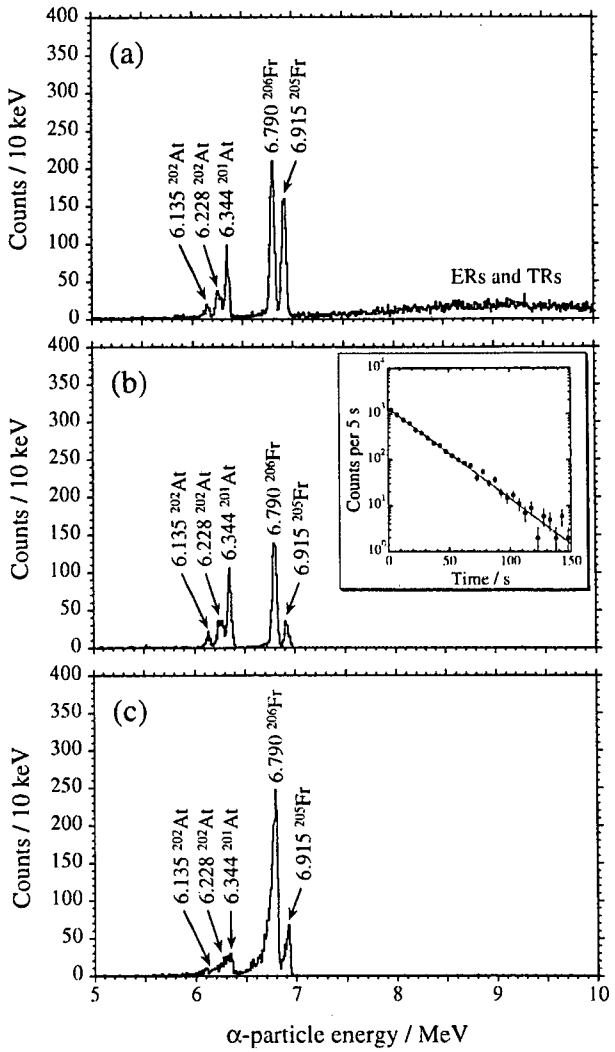

Figure 2. (a) Alpha-particle spectrum measured in the ^{206}Fr experiment for 2600 s in the 6th strip (middle) of the 12-strip Si detector (SD) under the beam-on condition. The ^{40}Ar beam intensity was 0.017 pμA. (b) Alpha-particle spectrum measured in the 6th strip of SD for 300 s after the 30-s beam irradiation. The inset shows a decay curve of the 6.790-MeV α peak of ^{206}Fr measured in all the strips of SD. The beam intensity was 1.9 pμA. (c) Alpha-particle spectrum measured in the first top detector of the rotating wheel system MANON for 30 s after the 30-s aerosol collection. The beam intensity was 1.8 pμA. The helium flow rate was 5 L min^{-1} and the chamber pressure was 90 kPa. The temperature of the KCl aerosol generator was 620 °C.

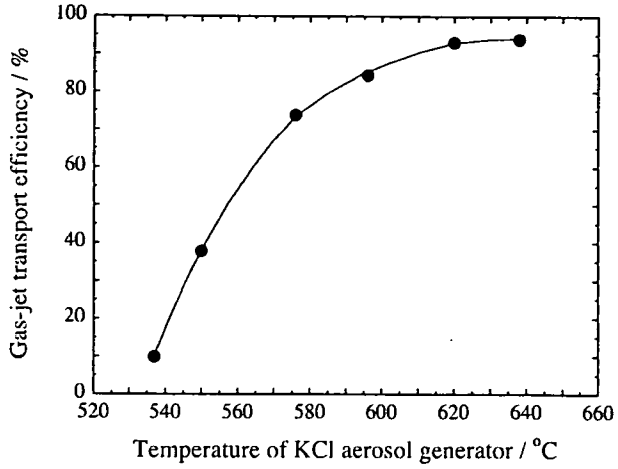

Figure 3. Variation of the gas-jet transport efficiency of ^{206}Fr as a function of the temperature of KCl aerosol generator. The helium flow rate was 5 L min^{-1} and the chamber pressure was 90 kPa. The ^{40}Ar beam intensity was 1.7 pμA.

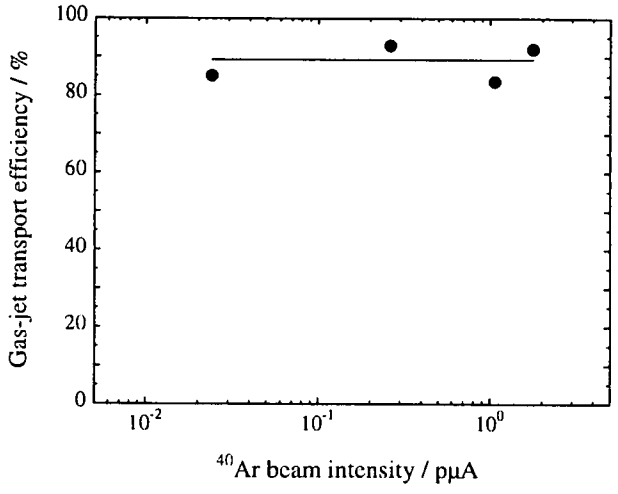

Figure 4. Variation of the gas-jet transport efficiency of ^{206}Fr as a function of the ^{40}Ar beam intensity. The helium flow rate was 5 L min^{-1} and the chamber pressure was 90 kPa. The temperature of the KCl aerosol generator was 620 °C.

the spectrum, indicating that the gas-jet transport of ^{206}Fr to MANON was successfully conducted after the physical separation by GARIS. The transport efficiency of the gas-jet system was evaluated using the 6.790-MeV α peak of ^{206}Fr.

In Figure 3, the gas-jet transport efficiencies of ^{206}Fr are shown as a function of the temperature of the KCl aerosol generator. The efficiency increases smoothly with an increase of the temperature and attain to over 90% at 620 °C. The variation of the gas-jet efficiencies of ^{206}Fr is shown in Figure 4 as a function of the ^{40}Ar beam intensity. The efficiencies are constant irrespectively of the beam intensities up to 2 pμA. In the conventional gas-jet system in that the beam passes through the target chamber, the gas-jet efficiency decreases due to the increasing plasma condition induced by the intense beam. As an example, we previously measured the gas-jet efficiencies of ^{173}W produced in the ^{nat}Gd(^{22}Ne,xn) reaction without the beam separation by GARIS. It was found that the gas-jet efficiency of ^{173}W drastically decreases from 40% at 6.6 pnA to 25% at 0.5 pμA with increasing beam intensity. Since the beam is separated by GARIS in the present experiment, such a decrease of the gas-jet efficiency is not observed for ^{206}Fr as shown in Figure 4.

Alpha-particle spectra of ^{245}Fm under the beam-on and beam-off conditions are shown in Figures 5(a) and 5(b), respectively. Although no α peaks are seen in the beam-on

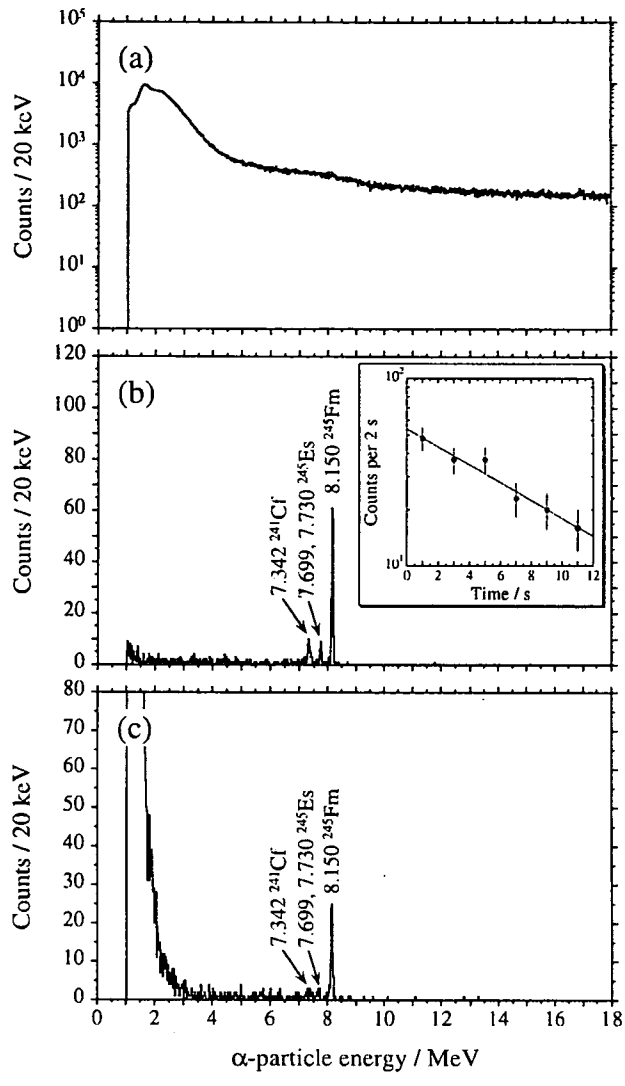

Figure 5. Sum of α-particle spectra measured in the ^{245}Fm experiment in the 12-strip Si detectors (SD) under (a) the beam-on and (b) beam-off conditions. The cycle of the beam-on (5 s) and beam-off (15 s) measurements was repeated 1265 times. The ^{40}Ar beam dose of 6.55 × 10^{16} was accumulated. The inset shows a decay curve of the 8.150-MeV α peak of ^{245}Fm. (c) Sum of α-particle spectra measured in the seven top detectors of the rotating wheel system MANON for 14 s after the 2-s aerosol collection. The 2-s aerosol collection was repeated 7289 times. The beam dose was 9.76 × 10^{16}. The helium flow rate was 5 L min^{-1} and the chamber pressure was 90 kPa. The temperature of the KCl aerosol generator was 620 °C.

spectrum (Figure 5(a)), α peaks of ^{245}Fm (4.2 s, 8.15 MeV)[17] and its daughter ^{241}Cf (3.78 min, 7.342 MeV)[17] are clearly seen in the beam-off spectrum (Figure 5(b)). The decay curve of the 8.15-MeV α peak is shown in the inset of Figure 5(b). The half-life of ^{245}Fm was determined to be 6.3 ± 1.3 s, which agrees with the literature value of 4.2 ± 1.3 s.[17] The α peaks around 7.7 MeV would be those of ^{245}Es (1.1 min, 7.699 and 7.730 MeV)[17] produced in the ^{208}Pb(^{40}Ar,p2n)^{245}Es reaction or the EC decay of ^{245}Fm. Background α-particles of, e.g., ^{211}Bi and ^{211m,212m}Po which are produced in the transfer reactions on the ^{208}Pb target[15] are completely removed by GARIS. The separation factors in excess of 10^4 were evaluated for ^{211}Bi and ^{211m,212m}Po based on their cross sections reported in Reference 15.

Compared in Figure 5(c) is the sum of α-particle spectra measured in the seven top detectors of MANON. The 8.15-MeV α peak of ^{245}Fm is clearly seen in the spectrum, and the gas-jet transport efficiency is determined to be 83 ± 9%. Despite of the physical separation by GARIS, one can see a lot of background events in Figure 5(c), especially below 4 MeV.

Since MANON was placed in the target room in this experiment, these background events were caused by large amounts of neutrons and/or γ rays during the irradiation. Very recently, we have constructed a chemistry laboratory isolated with a 50-cm concrete shield from the target room, where the background level is two orders of magnitude lower than that in the target room.

In this work, the high gas-jet efficiencies over 80% were obtained both for ^{206}Fr and ^{245}Fm. The recoil range of ^{206}Fr in helium at 90 k Pa is calculated to be 30 mm based on the SRIM 2006 code,[18] and that of ^{245}Fm is extrapolated to 18 mm from those of the lower Z ions (Z = 68–92) of A = 245. These recoil ranges are short enough as compared with the helium thickness of the gas-jet chamber used in this work (60 mm at 90 kPa). In the conventional gas-jet system in that the beam passes in the recoil chamber, the helium gas is swept out through the capillary outlet to the vertical direction of the beam axis. Therefore, the position of the capillary outlet in the chamber should be adjusted to the recoil ranges of the product nuclei of interest. Since the beam is separated by GARIS in the present system, we can put the capillary outlet at the center end of the chamber (see Figure 1(c)). Thus, helium gas is fed into the chamber through the four inlets directed to the surface of the Mylar window and is swept out thoroughly from the end of the chamber. In addition to the beam-free condition, this smooth helium flow in the chamber would be advantageous to the high gas-jet efficiency.

4. Summary and Perspectives

We have developed the gas-jet transport system coupled to GARIS as a preseparator for the SHE chemistry. The performance of the system was demonstrated using ^{206}Fr and ^{245}Fm produced in the ^{169}Tm(^{40}Ar,3n)^{206}Fr and ^{208}Pb(^{40}Ar,3n)^{245}Fm reactions, respectively. The α particles of ^{206}Fr and ^{245}Fm separated with GARIS and transported by the gas-jet were clearly observed with a rotating wheel system for α spectrometry. The high gas-jet efficiency of over 80% was found to be independent of the beam intensity up to 2 pμA. These results suggest that the GARIS/gas-jet system is a promising tool for future SHE chemistry at RIKEN. Recently, the gas-jet transport of ^{255}No produced in the ^{238}U(^{22}Ne,5n) reaction was also successful with the gas-jet efficiency over 80%. In the future, productions of SHE nuclides with long half-lives for chemical experiments such as ^{261}Rf, ^{262}Db, ^{265}Sg, ^{269}Hs, and ^{283}112 will be studied with the present system using ^{238}U and ^{248}Cm targets.

Acknowledgement. The authors express their gratitude to the crew of the RIKEN Linear Accelerator for their invaluable assistance in the course of these experiments. This research was partially supported by the REIMEI Research Resources of Japan Atomic Energy Research Institute, 2003, and by the Ministry of Education, Science, Sports and Culture, Grant-in-Aid for Young Scientists (B), 16750055, 2004–2006.

References

(1) *The Chemistry of Superheavy Elements*, Ed. M. Schädel, Kluwer Academic Publishers, Dordrecht (2003).
(2) M. Schädel, Angew. Chem. Int. Ed. **45**, 368 (2006).
(3) *6th Workshop on Recoil Separator for SHE Chemistry, Garching, Germany, September 29, 2006*: http://www-w2k.gsi.de/tasca06/.
(4) J. P. Omtvedt, J. Alstad, H. Breivik, J. E. Dyve, K. Eberhardt, C. M. Folden III, T. Ginter, K. E. Gregorich, E. A. Hult, M. Johansson, U. W. Kirbach, D. M. Lee, M. Mendel, A. Nähler, V. Ninov, L. A. Omtvedt, J. B. Partin, G. Skarnemark, L. Stavsetra, R. Sudowe, N. Wiehl, B. Wierczinski, P. A. Wilk, P. M. Zielinski, J. V. Kratz, N. Trautmann, H. Nitsche, and D. C. Hoffman, J. Nucl. Radiochem. Sci. **3**, 121 (2002).
(5) L. Stavsetra, K. E. Gregorich, J. Alstad, H. Breivik, K. Eberhardt, C. M. Folden III, T. N. Ginter, M. Johansson, U. W. Kirbach, D. M. Lee, M. Mendel, L. A. Omtvedt, J. B. Patin, G. Skarnemark, R. Sudowe, P. A. Wilk, P. M. Zielinski, H. Nitsche, D. C. Hoffman, and J. P. Omtvedt, Nucl. Instrum. Methods Phys. Res. A **543**, 509 (2005).
(6) Ch. E. Düllmann, G. K. Pang, C. M. Folden III, K. E. Gregorich, D. C. Hoffman, H. Nitsche, R. Sudowe, and P. M. Zielinski, *Advances in Nuclear and Radiochemistry, General and Interdisciplinary, Vol. 3*, Eds. S. M. Qaim and H. H. Coenen, Forschungszentrum Jülich GmbH, Jülich (2004), p 147.
(7) Ch. E. Düllmann, C. M. Folden III, K. E. Gregorich, D. C. Hoffman, D. Leitner, G. K. Pang, R. Sudowe, P. M. Zielinski, and H. Nitsche, Nucl. Instrum. Methods Phys. Res. A **551**, 528 (2005).
(8) R. Sudowe, M. G. Galvert, Ch. E. Düllmann, L. M. Farina, C. M. Folden III, K. E. Gregorich, S. E. H. Gallaher, D. C. Hoffman, S. L. Nelson, D. C. Phillips, J. M. Schwantes, R. E. Wilson, P. M. Zielinski, and H. Nitsche, Radiochim. Acta **94**, 123 (2006).
(9) U. W. Kirbach, C. M. Folden III, T. N. Ginter, K. E. Gregorich, D. M. Lee, V. Ninov, J. P. Omtvedt, J. B. Patin, N. K. Seward, D. A. Strellis, R. Sudowe, A. Türler, P. A. Wilk, P. M. Zielinski, D. C. Hoffman, and H. Nitsche, Nucl. Instrum. Methods Phys. Res. A **484**, 587 (2002).
(10) K. Morita, K. Morimoto, D. Kaji, H. Haba, E. Ideguchi, J. C. Peter, R. Kanungo, K. Katori, H. Koura, H. Kudo, T. Ohnishi, A. Ozawa, T. Suda, K. Sueki, I. Tanihata, H. Xu, A. V. Yeremin, A. Yoneda, A. Yoshida, Y.-L. Zhao, T. Zheng, S. Goto, and F. Tokanai, J. Phys. Soc. Jpn. **73**, 1738 (2004).
(11) K. Morita, K. Morimoto, D. Kaji, H. Haba, E. Ideguchi, R. Kanungo, K. Katori, H. Koura, H. Kudo, T. Ohnishi, A. Ozawa, T. Suda, K. Sueki, I. Tanihata, H. Xu, A. V. Yeremin, A. Yoneda, A. Yoshida, Y.-L. Zhao, and T. Zhen, Eur. Phys. J. A **21**, 257 (2004).
(12) K. Morita, K. Morimoto, D. Kaji, T. Akiyama, S. Goto, H. Haba, E. Ideguchi, K. Katori, H. Koura, H. Kudo, T. Ohnishi, A. Ozawa, T. Suda, K. Sueki, F. Tokanai, T. Yamaguchi, A. Yoneda, and A. Yoshida, J. Phys. Soc. Jpn. **76**, 043201 (2007).
(13) K. Morita, K. Morimoto, D. Kaji, T. Akiyama, S. Goto, H. Haba, E. Ideguchi, R. Kanungo, K. Katori, H. Koura, H. Kudo, T. Ohnishi, A. Ozawa, T. Suda, K. Sueki, H. Xu, T. Yamaguchi, A. Yoneda, A. Yoshida, and Y.-L. Zhao, J. Phys. Soc. Jpn. **73**, 2593 (2004).
(14) D. Vermeulen, H.-G. Clerc, C.-C. Sahm, K.-H. Schmidt, J. G. Keller, G. Münzenberg, and W. Reisdorf, Z. Phys. A **318**, 157 (1984).
(15) J. M. Nitschke, R. E. Leber, M. J. Nurmia, and A. Ghiorso, Nucl. Phys. **A313**, 236 (1979).
(16) Y. Nagame, M. Asai, H. Haba, S. Goto, K. Tsukada, I. Nishinaka, K. Nishio, S. Ichikawa, A. Toyoshima, K. Akiyama, H. Nakahara, M. Sakama, M. Schädel, J. V. Kratz, H. W. Gäggeler, and A. Türler, J. Nucl. Radiochem. Sci. **3**, 85 (2002).
(17) R. B. Firestone and V. S. Shirley, *Table of Isotopes, 8th ed.* John Wiley & Sons, New York (1996).
(18) J. F. Ziegler, *The Stopping and Range of Ions in Matter, SRIM*: http://www.srim.org/.

日本放射線技術学会画像分科会　画像通信　Vol.30(2),34-39

CdTeを用いたX線画像検出器モジュールの開発

（株）アクロラド
玉城　充　　三戸 美生　　首藤 靖浩
山口 浩司　　喜友名 達也　山本 雅也
寒河江 健一　喜名　徹

1．はじめに

従来、X線撮像装置として一般撮影などの静止画撮影においてはスクリーン-フィルムシステムや輝尽性蛍光体(イメージングプレートI.P)を用いたＣＲシステムが使用されてきたが、現像作業あるいはレーザー読出し作業が必要であるためリアルタイム性に欠けるといった面がある。また、フィルムの保管などの問題もある。一方、消化管系や血管造影などの透視撮影においてはイメージインテンシファイア(I.I)とＴＶカメラまたはＣＣＤカメラと組み合わせたＴＶ撮像システムが使用されてきたが、視野が円形であることや周囲部において画像の歪みが生じる。 またI.Iの電子レンズ部分は真空管で製作されているため装置の小型化には限界がある。このような背景のなか、近年フラットパネルディテクタ（Flat Panel Detector　以下 FPD）が登場し、既存のX線撮像装置で存在した問題が克服され、実際の臨床の現場で普及し始めている。特に従来では困難であった静止画撮影と透視撮影の両立が期待されている。またFPDの構造上、検出器部分の厚さを薄くできるために装置の小型化も容易になると思われる。

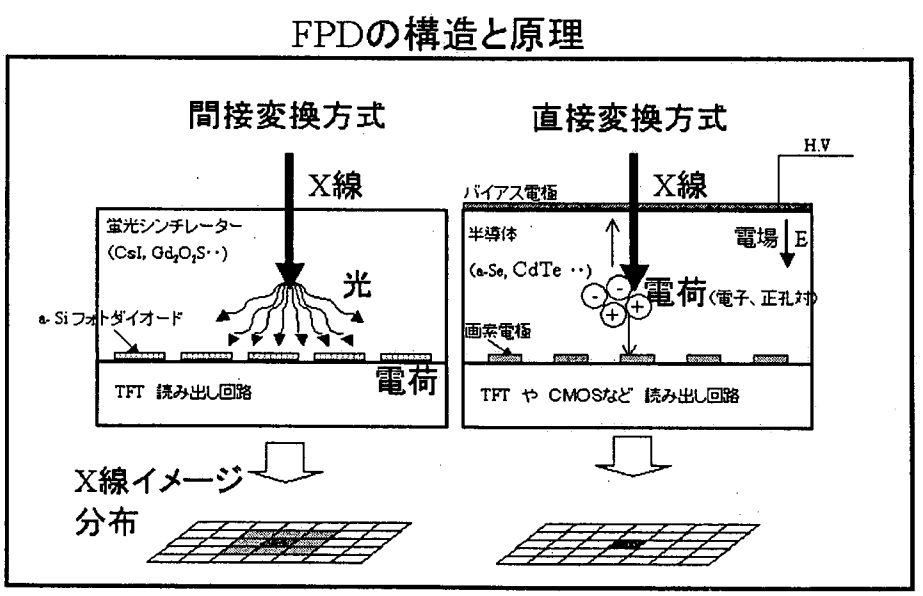

図1.FPDの構造と原理

現在、FPDと呼ばれるものは、入射X線を電荷に変換する原理の違いから間接変換方式と直接変換方式に大別される。図1にFPDの構造と原理を示す。間接変換方式の原理は、外部から入射す

るX線はCsIやGd_2O_2Sなどの蛍光シンチレーターによって一旦光に変換され、その後a-Siなどのフォトダイオードによって光から電荷に変換される。その後、蓄積された電荷はスイッチング機能を持つ薄膜トランジスタ(TFT)回路やCMOS回路などの読出し回路で信号として取り出される。この間接変換方式では原理上、シンチレーターの発光効率及びフォトダイオードの電荷変換効率による損失が起きるためX線検出感度に影響を及ぼす。また、シンチレーター内で光の散乱が起こるため、隣接ピクセルへの影響が避けられず、２次元画像上では、画像のボケが生じる。最近、シンチレーターを数μm径の柱状結晶にすることでボケを抑える工夫がされているが画素ピッチに相当する鮮鋭度は得ることは困難である。

一方、直接変換方式の原理は、入射したX線はアモルファスセレン(a-Se)やテルル化カドミウム(CdTe)などの半導体内で直接電荷に変換され、蓄積された電荷はTFTやCMOS回路で読み出される。この直接変換方式では最大の特徴は入射したX線は、直接電荷変化されるため極めて変換効率が良いこと、また半導体内には外部からの高電圧印加により高い電場が形成されており X線により生成された電子正孔対は直ちに対面電極へ収集されるため、ボケもなく鮮鋭度が非常に高いことである。このような背景から我々は、CdTe半導体を用いた直接変換方式のX線画像検出器モジュールを開発した。

2. CdTe半導体の特徴

CdTe 半導体の優れた特徴のひとつに原子番号と物質密度が比較的大きいために放射線に対する吸収効率が高いことが挙げられる。図２は単一エネルギー（80keV）を持つX線に対する吸収効率を示す。比較のために現在のFPDのX線変換部分に主に使用されているCsIシンチレーター、a-Se半導体も記載してある。厚さ1mmのCdTe半導体を用いた場合80keVのX線フォトンに対する吸収効率が80%以上であり、これはa-Se半導体の3～4mm厚にも相当する非常に高い検出効率であることがわかる。

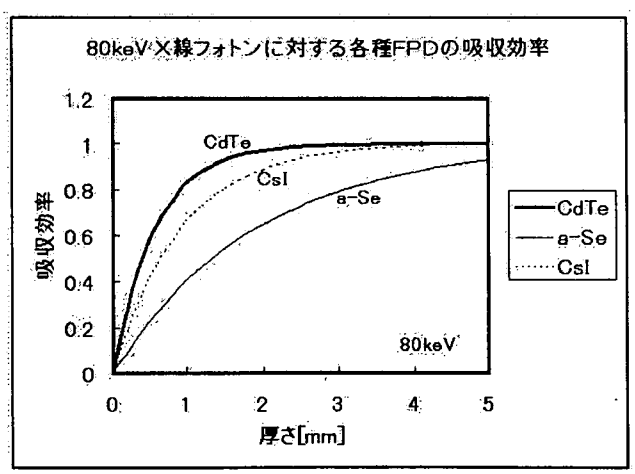

図２．80keVのＸ線に対する各種ＦＰＤの吸収効率

もうひとつの特徴は電子正孔対生成に必要なエネルギー値（以下W値）がa-Seにくらべて約1桁小さいことが挙げられる。一般に入射X線によって半導体内に生成される総電荷量は、各種半導体のW値に大きく依存し、W値が小さいほど生成電荷量が大きいことが知られている。CdTeとa-SeのW値の比較ではW(CdTe)=4.4eV、W(a-Se)=40～50eVであり、CdTeのほうが、より多い電荷量すなわち信号量が大きいため高感度のFPDとなる。ここでa-SeのW値は典型的な使用環境(X線エネルギー領域 60～100keV 、半導体内に形成される電場=10kV/mm)での値を引用している。CdTe 半導体が持つこれらの物理特性に加えて、我々は過去においてショットキー障壁型の電極形成に成功し、漏れ電流が低く且つ高いエネルギー分解能を持つCdTe放射線検出器の開発、製造に成功している。このため撮影部位の厚みの違いや組織を構成する物質の違いを敏感に検出できる高いコントラスト特性を持つ。我々はこのような優れた放射線検出特性を持つ CdTe半導体と信号読出集積回路(ASIC)を用いたハイブリッド接合型のX線画像検出器モジュールを開発した。

3．ハイブリッド接合型X線画像検出器モジュール

図3は我々が開発したX線画像検出器モジュールのX線検出部分を構成するCdTe－ASICハイブリッド接合型の画像検出素子の電極表面写真と断面図である。

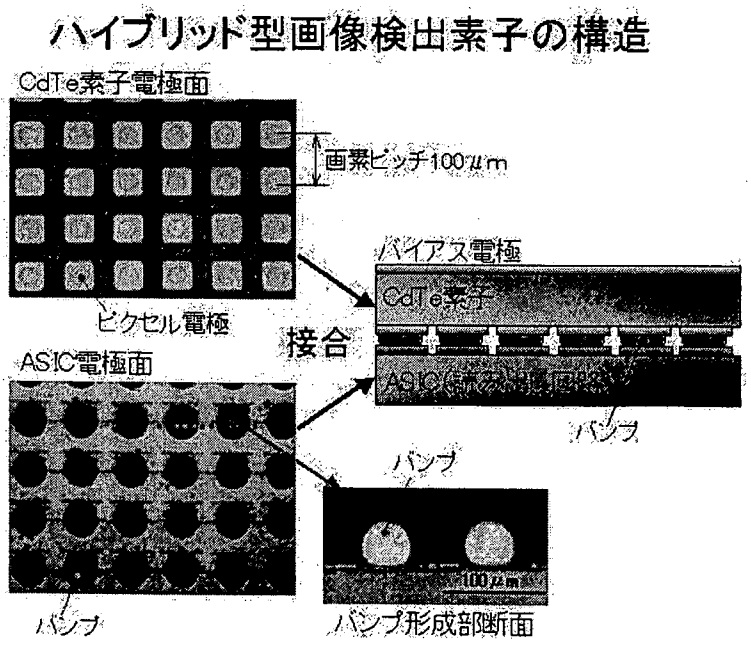

図3.ハイブリッド接合型X線検出器モジュール

X線変換部分には厚さ1mmの単結晶CdTeを使用しており、CdTe素子電極面には画素ピッチ100μm、画素数約3万のピクセル電極が形成されている。ASICは電荷積分型の機能を持っており入射X線によってCdTe素子内に生成される電荷を一定時間蓄積し放射線量値に比例した信号を出力するCMOS回路で構成されている。

CdTe素子とASIC間の接合には、100μmピッチの低融点ハンダバンプを用いフリップチップボンダ装置によってバンプ接合されている。このようなハイブリッド接合型の画像検出素子をアレイ状に4枚配置した開発試作品を製作した。図4に開発試作品の主な仕様と外観写真を示す。

X線画像検出器モジュール(開発試作品)

X線変換層	"単結晶"CdTe
厚さ	1mm
画素ピッチ	100 μm
画素数	~120,000
有効検出面積	23 × 50 mm²
通信インターフェース	USB・フレームグラバー
動画速度	50 fps(max)
出力データ	12bit

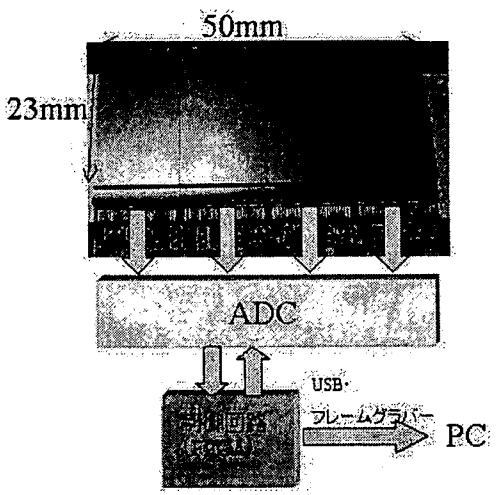

図4.開発試作品の仕様と外観写真

4．1　X線画像特性（入出力特性）

X線画像特性の評価項目としてX線入出力特性と鮮鋭度特性を測定した。

X線入出力特性は、マイクロフォーカスX線管（浜松ホトニクス製　X線焦点サイズ40μm）を使用し、タイムスケール法にて測定を行なった。照射条件は、フィルタなし、焦点—検出器間距離は60cm、管電圧80kV、管電流　0.1mA で測定を行った。図5の横軸は線量[mR]、縦軸は検出エリアに設定したROI内のピクセル平均値であり、両軸とも対数表示で示している。図からわかるように2桁程度のダイナミックレンジ領域で直線性をもつことが確認できる。

また、本開発試作品の他に透視撮影における典型的な線量領域（数μR～）に対応した低線量タイプの開発も現在すすめている。

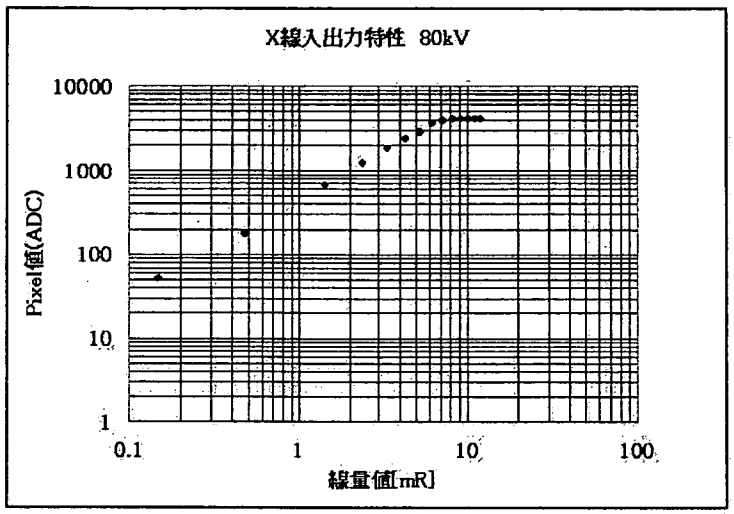

図５.X線入出力特性

４．２ X線画像特性（鮮鋭度特性）

鮮鋭度特性はX線テストチャートを用いて評価を行なった。撮影は同じX線管を使用し管電圧60kVにて撮影した。図６は同じ画素ピッチを持つ間接変換方式のFPD（CsI）と本開発試作品（CdTe）の比較である。100μmのナイキスト周波数5lp/mmにおいてCsIではボケが生じ、明確に認識できるのは3lp/mm程度が限界である。一方CdTeは、5lp/mmまで鮮明に識別できており、鮮鋭度特性が非常に優れていることがわかる。

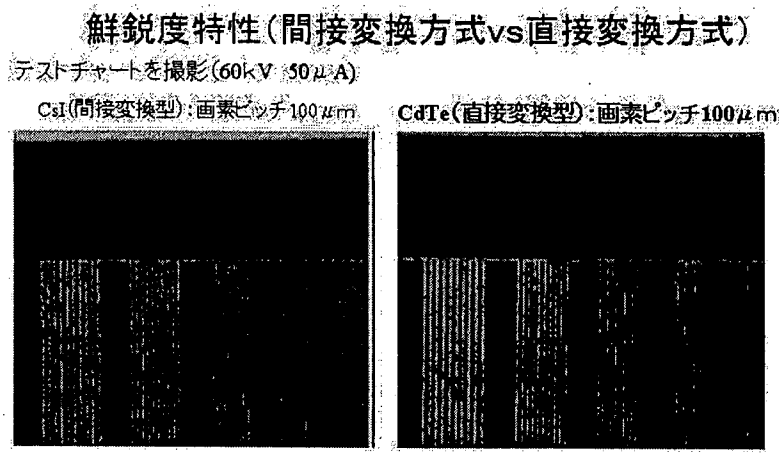

図６.鮮鋭度特性比較

5．応用例（歯科用パノラマ撮影）

図7は歯科用パノラマ撮影画像である。図7（a）は、従来のシンチレーター＋ＣＣＤで撮影されたもので、図7(b)は本開発品と同じCdTeを用いた直接変換方式の画像検出器（ただし300fpsの高速スキャン撮影タイプ）で撮影されたものである。CdTeで撮影された（b）のほうがボケがなく、より鮮明な画像であることが確認できる。

図7（a）シンチレーター＋ＣＣＤ

図7（b）CdTe

（写真提供 AJAT社）

6．おわりに

放射線検出特性に優れたCdTe半導体と読出集積回路（ASIC）とをバンプ接合したハイブリッド型のX線画像検出器モジュールを自社開発した。開発試作品のX線画像評価の結果、特に鮮鋭度特性において間接変換方式と比較して非常に高い鮮鋭度を持つことを確認した。現在、更なる画質の向上と検出器エリアの拡大に向けて開発を進めている。

(19)日本国特許庁(JP)　(12)公開特許公報(A)　(11)特許出願公開番号
特開2008-45948
(P2008-45948A)
(43)公開日　平成20年2月28日(2008.2.28)

(51)Int.Cl.			F I			テーマコード（参考）
G01T	1/24	(2006.01)	G01T	1/24		2G088
G01T	7/00	(2006.01)	G01T	7/00	A	
G01T	1/161	(2006.01)	G01T	1/161	C	

審査請求 未請求　請求項の数 4　OL　（全 14 頁）

(21)出願番号　特願2006-220446 (P2006-220446)
(22)出願日　平成18年8月11日 (2006.8.11)

(71)出願人　503359821
独立行政法人理化学研究所
埼玉県和光市広沢２番１号
(74)代理人　100091096
弁理士　平木　祐輔
(74)代理人　100105463
弁理士　関谷　三男
(74)代理人　100102576
弁理士　渡辺　敬章
(72)発明者　本村　信治
埼玉県和光市広沢２番１号　独立行政法人理化学研究所内
(72)発明者　榎本　秀一
埼玉県和光市広沢２番１号　独立行政法人理化学研究所内

最終頁に続く

(54)【発明の名称】ガンマ線検出装置

(57)【要約】
【課題】検出できるエネルギーレンジを拡大したガンマ線検出装置を提供する。
【解決手段】ガンマ線との相互作用位置及びエネルギーを検出できる一対の高エネルギーガンマ線用の位置感応型ガンマ線検出器１０２，１０３の前方に、ガンマ線との相互作用位置及びエネルギーを検出できる低エネルギーガンマ線用の位置感応型ガンマ線検出器１０１を配置する。
【選択図】図３

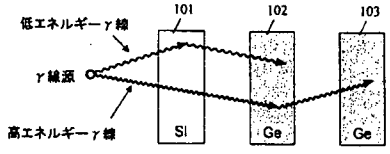

【特許請求の範囲】
【請求項１】
ガンマ線との相互作用位置及びエネルギーを検出できる一対の高エネルギーガンマ線用の位置感応型ガンマ線検出器と、
その前方に配置された、ガンマ線との相互作用位置及びエネルギーを検出できる低エネルギーガンマ線用の位置感応型ガンマ線検出器と
を備えることを特徴とするガンマ線検出装置。
【請求項２】
請求項１記載のガンマ線検出装置において、前記高エネルギーガンマ線用の位置敏感型ガンマ線検出器はゲルマニウム結晶を備え、前記低エネルギーガンマ線用の位置敏感型ガンマ線検出器はシリコン結晶を備えることを特徴とするガンマ線検出装置。
【請求項３】
請求項１又は２記載のガンマ線検出装置において、前記低エネルギーガンマ線用の位置感応型ガンマ線検出器は、エネルギー１００ｋｅＶのガンマ線に対するコンプトン散乱の生起確率が高エネルギーガンマ線用の位置感応型ガンマ線検出器より高く、エネルギー１０００ｋｅＶのガンマ線に対するコンプトン散乱の生起確率が高エネルギーガンマ線用の位置感応型ガンマ線検出器より低いことを特徴とするガンマ線検出装置。
【請求項４】
請求項１～３のいずれか１項記載のガンマ線検出装置において、前記３個の位置敏感型ガンマ線検出器のうちの２個だけでガンマ線の相互作用を検出した事象のみを取り出す同時計測回路を有することを特徴とするガンマ線検出装置。
【発明の詳細な説明】
【技術分野】
【０００１】
本発明はガンマ線検出装置に関し、特にガンマ線の飛来方向を検出することのできるガンマ線検出装置に関する。
【背景技術】
【０００２】
コリメータを用いることなくガンマ線の飛来方向あるいはガンマ線源の位置を検出することのできるガンマ線検出装置として、コンプトン散乱の運動学を利用するガンマ線検出装置が特開平９－１０１３７１号公報や特開２００５－２０８０５７号公報に記載されている。このガンマ線検出装置は、位置分解能及びエネルギー分解能を有する２枚のゲルマニウム検出器を用い、前方のゲルマニウム検出器に入射してコンプトン散乱された後、後方のゲルマニウム検出器に入射して吸収されたガンマ線検出事象に着目し、２つのゲルマニウム検出器におけるガンマ線の検出位置及び検出エネルギーをもとにガンマ線源の存在する方向あるいは位置を演算するものである。T. Tanaka et al.：”Development of a Si/CdTe semiconductor Compton telescope”, Proceedings of SPIE 5501(2004) pp.229-240.には、シリコン検出器とテルル化カドミウム（ＣｄＴｅ）検出器を組み合わせ、同様の原理を応用したガンマ線天文学用の撮像装置が記載されている。
【０００３】
【特許文献１】特開平９－１０１３７１号公報
【特許文献２】特開２００５－２０８０５７号公報
【非特許文献１】Proceedings of SPIE 5501(2004) pp.229-240.
【発明の開示】
【発明が解決しようとする課題】
【０００４】
２枚のゲルマニウム検出器を用いるガンマ線検出装置は、広いエネルギー範囲のガンマ線を検出可能である。しかしながら、ガンマ線のエネルギーが低くなると、ゲルマニウム結晶中で光電吸収が起こる確率が高くなり、コンプトン散乱を利用するガンマ線の検出感度が低下する。図１は、ガンマ線のエネルギーをパラメータとして、コンプトン散乱の生

起確率とゲルマニウムの厚さとの関係を示した図である。図から分かるように、ガンマ線のエネルギーが１００ｋｅＶ程度まで低くなると、どんなにゲルマニウム結晶を厚くしたとしてもコンプトン散乱の起こる確率は２割程度にとどまり、検出効率が著しく低下してしまう。また、Proceedings of SPIE 5501(2004) pp.229-240.に記載されているように、前面の検出器をシリコン半導体検出器にすると、ゲルマニウムに比べて、より低いエネルギーのガンマ線に対してもコンプトン散乱の生起確率を向上させることができる。しかしながらこの場合は、約２００ｋｅＶ以上のガンマ線はシリコン検出器を透過し易くなり、コンプトン散乱の生起確率が低下してしまう。

【０００５】

本発明は、検出できるエネルギーレンジを拡大したガンマ線検出装置を提供することを目的とする。

【課題を解決するための手段】

【０００６】

２枚の位置感応型のゲルマニウム検出器の前方に、さらに位置感応型のシリコン検出器を追加する。そうすると、低いエネルギーのガンマ線のコンプトン散乱は主にシリコン検出器で起こり、散乱されたガンマ線は後方のゲルマニウム検出器で検出される。また、高いエネルギーのガンマ線はシリコン検出器を透過しやすくなるので、主に次段のゲルマニウム検出器中でコンプトン散乱され、散乱されたガンマ線は最後方の検出器で検出される。従って、低エネルギーから高エネルギーまでのガンマ線を高効率で撮像することが可能になる。これによって、２枚のゲルマニウム検出器を用いたガンマ線撮像装置では撮像が難しかった低エネルギーのガンマ線を放出するインビボ診断用のＳＰＥＣＴ核種の撮像も可能になる。

【０００７】

図２は、ゲルマニウム結晶とシリコン結晶中におけるコンプトン散乱の生起確率と結晶の厚さとの関係を示した図である。この図から明らかなように、１段目の検出器の素材をシリコンにすれば、エネルギーが１００ｋｅＶ程度のガンマ線でもコンプトン散乱の生起確率を向上することができる。従って、１段目の検出器をシリコン、２段目の検出器をゲルマニウムやＣｄＴｅにすることが考えられる。しかし、ガンマ線のエネルギーが約２００ｋｅＶ以上になると、シリコンよりもゲルマニウムの方がコンプトン散乱の生起確率が高いために、Ｓｉ＋ＣｄＴｅなどの装置は高エネルギーのガンマ線の検出には向かない。

【０００８】

そこで本発明では、相対的に高エネルギーのガンマ線に対するコンプトン散乱の生起確率が高いガンマ線検出器（以下、高エネルギー用ガンマ線検出器という）を２枚配置した前方に、相対的に低エネルギーのガンマ線に対するコンプトン散乱の生起確率が高いガンマ線検出器（以下、低エネルギー用ガンマ線検出器という）を配置した構成を採用する。

【０００９】

すなわち、本発明のガンマ線検出装置は、ガンマ線との相互作用位置及びエネルギーを検出できる一対の高エネルギーガンマ線用の位置感応型ガンマ線検出器と、その前方に配置された、ガンマ線との相互作用位置及びエネルギーを検出できる低エネルギーガンマ線用の位置感応型ガンマ線検出器とを備える。高エネルギーガンマ線用の位置敏感型ガンマ線検出器はゲルマニウム結晶を備え、低エネルギーガンマ線用の位置敏感型ガンマ線検出器はシリコン結晶を備えるものとすることができる。

【００１０】

低エネルギーガンマ線用の位置感応型ガンマ線検出器は、典型的には、エネルギー１００ｋｅＶのガンマ線に対するコンプトン散乱の生起確率が高エネルギーガンマ線用の位置感応型ガンマ線検出器より高く、エネルギー１０００ｋｅＶのガンマ線に対するコンプトン散乱の生起確率が高エネルギーガンマ線用の位置感応型ガンマ線検出器より低い検出器とすることができる。

【発明の効果】

【００１１】

本発明によると、低エネルギーのガンマ線から高エネルギーのガンマ線まで広いエネルギーレンジにわたって高い効率で検出することができる。

【発明を実施するための最良の形態】

【００１２】

以下、図面を参照して本発明の実施の形態を説明する。

図３は、本発明によるガンマ線検出装置におけるガンマ線検出器の配置を示す模式図である。本発明によるガンマ線検出装置は、ガンマ線の入射側から、１段目の検出器１０１、２段目の検出器１０２、３段目の検出器１０３を順に平行に並べて配置した構造を有する。１段目の検出器１０１はシリコン半導体検出器からなる低エネルギー用ガンマ線検出器である。２段目の検出器１０２及び３段目の検出器１０３は、それぞれゲルマニウム半導体検出器からなる高エネルギー用ガンマ線検出器である。１段目の検出器１０１の材質はダイヤモンドとしてもよい。また、３段目の検出器１０３は、より原子番号が大きなＣｄＴｅ検出器あるいはＣｄＺｎＴｅ検出器などで代用することもできる。各ガンマ線検出器は、以下に説明するような原理でガンマ線との相互作用点の位置と相互作用によって検出器に与えられたエネルギーを測定可能な、位置感応型半導体検出器である。

【００１３】

ガンマ線源から放出された１００ｋｅＶ程度の低いエネルギーのガンマ線は主に１段目のシリコン検出器でコンプトン散乱される。その散乱されたガンマ線が２段目または３段目のゲルマニウム検出器で光電吸収されたとすると、それぞれの検出器で測定されたエネルギーをコンプトン散乱の運動学方程式に代入して散乱角を求めることができる。つまり、計測された２つの相互作用点を通る直線を軸とし、１段目の検出器中の相互作用点を頂点とした、散乱角の２倍の開角円錐が定まる。また、ガンマ線源から放出された約２００ｋｅＶ以上の高いエネルギーのガンマ線は１段目のシリコン検出器を透過しやすくなり、主に２段目のゲルマニウム検出器でコンプトン散乱される。その散乱されたガンマ線が３段目の検出器で光電吸収されたとすると、低エネルギーガンマ線の場合と同様に、計測された２つの相互作用点を通る直線を軸とし、２段目の検出器中の相互作用点を頂点とした、散乱角の２倍の開角円錐が定まる。すなわち、コンプトンカメラ方式によって低エネルギーから高エネルギーまでのガンマ線を高効率で撮像することが可能になる。

【００１４】

次に、本発明のガンマ線検出装置によるガンマ線源の検出原理について説明する。ここでは、ガンマ線の相互作用を検出した２つの検出器のうち、ガンマ線源により近い方の検出器でコンプトン散乱され、ガンマ線源からより遠い方の検出器で光電吸収された事象に着目し、前者の検出器を散乱検出器、後者の検出器を吸収検出器と呼ぶ。図３に示した検出器のうち、１段目の検出器１０１あるいは２段目の検出器１０２が散乱検出器となりうる。１段目の検出器１０１が散乱検出器の場合、吸収検出器となりうるのは２段目の検出器１０２と３段目の検出器１０３である。また、２段目の検出器１０２が散乱検出器の場合、吸収検出器となりうるのは３段目の検出器１０３である。

【００１５】

図４は、散乱検出器と吸収検出器によるガンマ線源の検出原理を示した図である。

図示したガンマ線１４，１５は、散乱検出器１１に入射してそこでコンプトン散乱された後、吸収検出器１２に入射してそこで全エネルギーを失ったものであり、本発明ではこのような事象に注目する。なお、ガンマ線１４とガンマ線１５は別々の時間に検出部１０に入射したものとする。

【００１６】

この時、例えばガンマ線１４は前方の散乱検出器１１にE_1のエネルギーを付与し、後方の吸収検出器１２にE_2のエネルギーを付与するため、次式（１）の関係が成り立つ。

【００１７】

$$E = E_1 + E_2 \qquad (1)$$

【００１８】

この測定されたエネルギーＥによって核種を識別することができる。そして、コンプト